

Swarthmore College

Works

Chemistry & Biochemistry Faculty Works

Chemistry & Biochemistry

11-22-2005

Second OH Overtone Excitation And Statistical Dissociation Dynamics Of Peroxynitrous Acid

I. M. Konen

E. X.J. Li

Thomas Alex Stephenson
Swarthmore College, tstephe1@swarthmore.edu

See next page for additional authors

Follow this and additional works at: <https://works.swarthmore.edu/fac-chemistry>

 Part of the [Physical Chemistry Commons](#)

[Let us know how access to these works benefits you](#)

Recommended Citation

I. M. Konen, E. X.J. Li, Thomas Alex Stephenson, and M. I. Lester. (2005). "Second OH Overtone Excitation And Statistical Dissociation Dynamics Of Peroxynitrous Acid". *Journal Of Chemical Physics*. Volume 123, Issue 20. DOI: 10.1063/1.2126968
<https://works.swarthmore.edu/fac-chemistry/15>

This work is brought to you for free by Swarthmore College Libraries' Works. It has been accepted for inclusion in Chemistry & Biochemistry Faculty Works by an authorized administrator of Works. For more information, please contact myworks@swarthmore.edu.

Authors

I. M. Konen, E. X.J. Li, Thomas Alex Stephenson, and M. I. Lester

Second OH overtone excitation and statistical dissociation dynamics of peroxytrous acid

Ian M. Konen, Eunice X. J. Li, Thomas A. Stephenson, and Marsha I. Lester

Citation: *The Journal of Chemical Physics* **123**, 204318 (2005); doi: 10.1063/1.2126968

View online: <http://dx.doi.org/10.1063/1.2126968>

View Table of Contents: <http://scitation.aip.org/content/aip/journal/jcp/123/20?ver=pdfcov>

Published by the [AIP Publishing](#)



Re-register for Table of Content Alerts

Create a profile.



Sign up today!



Second OH overtone excitation and statistical dissociation dynamics of peroxyxynitrous acid

Ian M. Konen, Eunice X. J. Li, Thomas A. Stephenson,^{a)} and Marsha I. Lester^{b)}
Department of Chemistry, University of Pennsylvania, Philadelphia, Pennsylvania 19104-6323

(Received 11 August 2005; accepted 28 September 2005; published online 29 November 2005)

The second OH overtone transition of the *trans-perp* conformer of peroxyxynitrous acid (tp-HOONO) is identified using infrared action spectroscopy. HOONO is produced by the recombination of photolytically generated OH and NO₂ radicals, and then cooled in a pulsed supersonic expansion. The second overtone transition is assigned to tp-HOONO based on its vibrational frequency (10 195.3 cm⁻¹) and rotational band contour, which are in accord with theoretical predictions and previous observations of the first overtone transition. The transition dipole moment associated with the overtone transition is rotated considerably from the OH bond axis, as evident from its hybrid band composition, indicating substantial charge redistribution upon OH stretch excitation. The overtone band exhibits homogeneous line broadening that is attributed to intramolecular vibrational redistribution, arising from the coupling of the initially excited OH stretch to other modes that ultimately lead to dissociation. The quantum state distributions of the OH X ²Π ($\nu=0$) products following first and second OH overtone excitation of tp-HOONO are found to be statistical by comparison with three commonly used statistical models. The product state distributions are principally determined by the tp-HOONO binding energy of 16.2(1) kcal mol⁻¹. Only a small fraction of the OH products are produced in $\nu=1$ following the second overtone excitation, consistent with statistical predictions. © 2005 American Institute of Physics.
 [DOI: 10.1063/1.2126968]

I. INTRODUCTION

The three-body association reaction of OH with NO₂ to produce stable nitric acid (HONO₂),



is a key termination step of the radical chemistry that occurs in the lower atmosphere.¹ This process terminates many reactions involving HO_x (HO_x ≡ OH + HO₂) and NO_x (NO_x ≡ NO + NO₂) species that would otherwise lead to photochemical smog. Until recently, this intramolecular reaction was believed to produce HONO₂ exclusively, but kinetic studies over a wide range of pressure (for the bath gas M) and temperature conditions have shown that a secondary reaction product is also formed.²⁻⁵ The secondary product was proposed to be peroxyxynitrous acid (HOONO),^{2,6,7} a weakly bound isomer of HONO₂. Under atmospheric conditions, HOONO is formed reversibly,



and is estimated to account for up to 20% of the yield from the OH + NO₂ reaction.⁵

Ab initio studies have predicted that there are at least two stable conformations of HOONO,^{5,8-10} namely, the *trans-perp* (tp) conformer with an extended open structure and the *cis-cis* (cc) conformer with a five-member ringlike structure.

The latter has an intramolecular hydrogen bond between the terminal hydrogen and oxygen atoms, which increases the rigidity and stability of the cc conformer, and also has the effect of significantly shifting its OH stretching frequency to lower energy. As illustrated in Fig. 1, experiments have shown that the tp-conformer has a stability of 16.2(1) kcal mol⁻¹ relative to the OH + NO₂ asymptote,¹¹ the cc conformer has a stability of ~19.8 kcal mol⁻¹,^{4,12} and a substantial barrier (tp-cc) separates the two conformers.¹³ There has been considerable debate in the literature (as yet unresolved) as to whether or not there is a third stable conformer of HOONO in the *cis-perp* (cp) configuration.^{8,9,13-15} Nevertheless, there is ample evidence that torsional excitation of cc-HOONO can break the intramolecular hydrogen bond and thereby access cp-like configurations.^{12,16}

Although HOONO was detected under matrix-isolation conditions some time ago,^{17,18} it eluded gas-phase spectroscopic detection until very recently. The cc-HOONO conformer has been subsequently observed under thermal flow cell conditions using infrared action spectroscopy in the first and second OH overtone regions,^{13,19,20} cavity ring down spectroscopy in the fundamental and first OH overtone regions,^{10,16} and pure rotational spectroscopy.²¹ The tp-HOONO conformer has been characterized by this laboratory using infrared action spectroscopy in the first OH overtone region under jet-cooled conditions,^{11,22} and has also been detected using this same method under thermal conditions.¹³ The cc-HOONO conformer was not detected in the first overtone region under analogous jet-cooled conditions,¹¹ because a combination of its lower OH over-

^{a)}On sabbatical leave (2004-2005) from the Department of Chemistry and Biochemistry, Swarthmore College, Swarthmore, PA 19081.

^{b)}Author to whom correspondence should be addressed. Fax: (215) 573-2112; electronic mail: milester@sas.upenn.edu

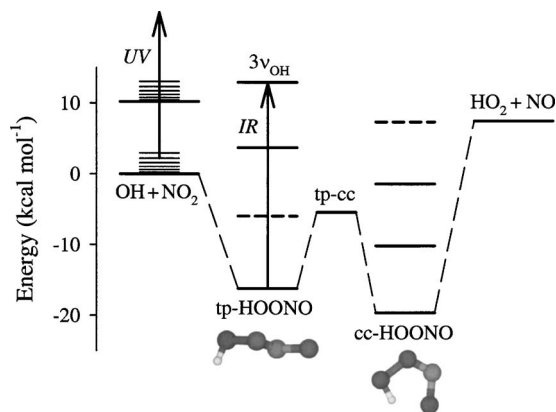


FIG. 1. Potential energy diagram for the *trans-perp* (tp) and *cis-cis* (cc) conformers of peroxyxynitrous acid (HOONO), illustrating the OH+NO₂ and HO₂+NO asymptotes along with the tp-cc isomerization barrier. The second OH overtone of tp-HOONO is excited by the IR pump laser and the OH ($\nu=0$) or ($\nu=1$) fragments are detected with the UV probe laser. The previously observed HOONO vibrational transitions are marked with solid lines (Refs. 10, 11, 13, 16, 19, 20, and 22), while unobserved or tentatively assigned vibrational transitions are indicated as dashed lines (Ref. 20). The stability of tp-HOONO of 16.2(1) kcal mol⁻¹ is taken from Ref. 11, while that for cc-HOONO is obtained from Refs. 4 and 12.

tone transition frequency, 6365 cm⁻¹ (cc) vs 6971 cm⁻¹ (tp), and greater binding energy prevents dissociation, which is required for action spectroscopy measurements. The cc-HOONO overtone spectrum obtained under thermal conditions also exhibits a reduced quantum yield for features below ~ 6940 cm⁻¹ (19.8 kcal mol⁻¹).¹³ This skews the appearance of the action spectrum, suppressing lower energy features relative to hot bands originating from excited torsional levels that appear at higher frequency (~ 6935 cm⁻¹).^{12,16}

This paper extends our previous work^{11,22} by examining HOONO in the second OH overtone region under jet-cooled conditions. The overtone transition associated with the tp conformer is identified by its vibrational frequency and rotational band contour. Other aspects of the overtone spectrum provide detailed information on the transition dipole moment and the initial step of the intramolecular vibrational redistribution process that ultimately leads to dissociation. Finally, the quantum state distributions of the OH products resulting from first and second OH overtone excitation of tp-HOONO are thoroughly characterized and compared with the predictions of several commonly used statistical models.

II. EXPERIMENTAL METHOD

The second OH overtone transition of tp-HOONO is detected in a pulsed supersonic expansion using an IR pump-UV probe technique similar to that used previously for the first OH overtone transition.^{11,22} For the second overtone, IR excitation occurs at 0.98 μ m and leads to the dissociation of tp-HOONO. The OH fragments are then detected by UV laser-induced fluorescence. Two types of experiments are performed: (1) Infrared action spectra of tp-HOONO ($3\nu_{\text{OH}}$) are recorded by scanning the IR pump laser with the UV laser fixed on a specific OH transition and (2) OH (ν, J_{OH}) quantum state distribution is determined by tuning

the UV probe laser to various OH $A^2\Sigma^+ - X^2\Pi$ transitions with the IR pump laser fixed on the tp-HOONO overtone transition.

The procedure for generating HOONO in a pulsed supersonic expansion has been described previously,¹¹ and only a brief summary is given here. The vapor from nitric acid (HONO₂, 100% fuming, Spectrum Laboratory Products, Inc.) is entrained in Ar carrier gas (80 psi) and then photolyzed with the 193 nm output of an ArF excimer laser (Lambda Physik, Complex 102). Photolysis takes place within a quartz capillary tube (Wilma Labglass, Suprasil 300, 0.5 mm (i.d.) \times 5 mm (o.d.) \times 10 mm length) attached to a solenoid pulsed valve assembly (Parker Hannifin, Series 9). The photolytically generated OH and NO₂ radicals undergo three-body association reactions in the high-pressure environment of the quartz capillary tube, leading to regeneration of HONO₂ as well as formation of the desired HOONO product. Most of the OH radicals are reacted away in flowing through the capillary when photolysis occurs close to the pulsed valve, significantly reducing the OH background relative to other photolysis positions.¹¹ The newly formed HOONO and other species present in the gas mixture are subsequently cooled in the supersonic expansion.

Infrared radiation at 0.98 μ m is produced with a β -BaB₂O₄ (BBO)-based optical parametric oscillator (OPO, Continuum Sunlite) pumped by the 355 nm output of an injection-seeded Nd: yttrium aluminum garnet (YAG) laser (Continuum Precision 9010, 6 ns pulse and 10 Hz repetition rate). The OPO has a 0.12 cm⁻¹ bandwidth [full width at half maximum (FWHM)] and is typically stepped in 0.03 cm⁻¹ increments for each IR scan. The idler output of the OPO has a pulse energy of ~ 17 mJ at the desired wavelength.

The absolute frequency of the IR source is determined by taking a photoacoustic spectrum of H₂O using the idler output of the OPO. The observed photoacoustic transitions are compared with well-documented H₂O lines in this spectral region.²³ Higher precision relative frequency markers are also generated by recording an etalon trace using a portion of the signal output from the OPO. The relative frequency scale is determined by linear interpolation between adjacent etalon fringes (free spectral range = 1.68 cm⁻¹). Frequency calibrations are taken concurrently with each IR spectrum of HOONO.

The second overtone excitation of tp-HOONO provides sufficient energy to produce both OH ($\nu=0$) and ($\nu=1$) fragments, which are separately probed using $A-X$ (1,0) and (0,1) transitions, respectively. The UV probe beam is generated by frequency doubling (Continuum UVT) the output of a Nd:YAG-pumped dye laser (Continuum 7020 and ND 6000, 7 ns pulse and 20 Hz repetition rate). The UV radiation for the (1,0) transition at 282 nm is obtained by operating the dye laser with Rhodamine 590 dye or Rhodamine 590/610 dye mixture, and that for the (0,1) transition at 346 nm is achieved with LDS 698 dye. Typically, ~ 1 mJ/cm² of UV radiation is passed into the vacuum chamber with each pulse. The UV laser is calibrated using well-known positions of the OH $A-X$ (1,0) or (0,1) lines.^{24,25}

The IR pump and UV probe beams are counterpropagated into the vacuum apparatus, where they are spatially

overlapped 1.0 cm (or ~ 20 nozzle diameters) downstream from the exit of the quartz capillary tube. This distance has been reduced from 1.5 cm in previous studies^{11,22} to increase the number density of HOONO in the laser interaction region. The IR-UV time delay is also reduced from 50 to 20 ns to make certain that there are no collisions between the IR excitation of HOONO and the arrival of the UV probe laser. The HOONO spectra are recorded with the IR beam focused to ~ 3 mm diameter, with the UV beam unfocused but reduced to ~ 1 mm diameter with an aperture.

The OH laser-induced fluorescence (LIF) signal originating from the laser interaction region is collected using $f/1$ optics and detected with a photomultiplier tube (PMT, EMI 9813Q) positioned perpendicular to both the laser and supersonic expansion axes. Scattered laser light from the photolysis and UV probe lasers is removed by a long pass filter (Schott WG-280) and a bandpass filter (14 nm FWHM) centered at either 307 nm for the OH $A-X$ (0,0) emission or 315 nm for the (1,1) emission. Filter transmission curves were measured with a UV/V is spectrophotometer (Beckman-Coulter DU640) to take into account the transmission of the filters at the OH $A^2\Sigma^+$ emission wavelengths in the data analysis. The PMT signal is amplified, integrated over a 400 ns gate, and transferred to a laboratory computer for further analysis.

The IR pump laser (10 Hz) is present for every other UV probe laser pulse (20 Hz). The HOONO infrared spectra are recorded using an active background subtraction procedure. Any background signal arising from the UV laser alone is subtracted from the IR+UV signal on every other laser shot.

The OH product state distribution is examined for both $\nu=0$ and $\nu=1$ vibrational levels. More extensive studies are carried out for OH ($\nu=0$), where Q_1 , Q_2 , P_1 , and P_2 (or R_1 and R_2) branches are measured on the $A-X$ (1,0) transition, whereas only the Q_1 branch of the $A-X$ (0,1) transition is probed for OH ($\nu=1$). These particular transitions have been chosen in order to examine the relative population of the OH fragments as a function of vibrational (ν), rotational (J_{OH}), spin-orbit (Ω), and lambda-doublet (Λ) states. Neither Λ -doublet component, $\Pi(A')$, or $\Pi(A'')$, of the lowest rotational state, OH $^2\Pi_{3/2}$ ($\nu=0$, $J_{OH}=3/2$), could be probed due to its large background population in the supersonic expansion. In addition, the population in a few OH ($\nu=0$) rotational levels that are probed by the $A-X$ (1,0) $Q_1(13/2)$, $Q_2(1/2)$, and $Q_2(7/2)$ lines cannot be distinguished due to overlapping transition frequencies. Finally, nearby weak satellite lines (P_{21} and Q_{21}) may partially overlap main branch lines (Q_1 and R_1) for the lowest J_{OH} .^{24,25}

For the OH product state data, the UV laser is fixed on a specific OH transition and the LIF signal is collected with the IR laser on then off (750 laser shots on then off) in three independent measurements that are separately averaged. The IR-induced signal is taken to be the difference between the averaged IR on and off values. The intensity observed for each OH product transition is scaled relative to a reference line in each vibrational state, namely, either the $A-X(1,0) Q_1(9/2)$ or $A-X(0,1) Q_1(5/2)$ line, which is recorded immediately before and after each transition in order

to account for small variations in the experimental conditions. These particular reference lines are selected because of their optimal signal-to-background ratios.

We have improved our analysis procedures for converting saturated LIF intensities measured on various OH $A-X$ (1,0) or (0,1) lines into ground $X^2\Pi$ ($\nu=0$ or 1) state populations. The improvements take into account the transmission properties of the bandpass filters used in collecting OH $A-X$ (1,1) or (0,0) fluorescence as well as the total lifetime and fluorescence quantum yield of the emitting state. These changes were needed because unimolecular dissociation of tp-HOONO ($3\nu_{OH}$) produces OH $X^2\Pi$ fragments in a broad range of quantum states. Subsequent LIF detection then accesses a correspondingly broad range of OH $A^2\Sigma^+$ ($\nu=0$ or 1) quantum states, some of which are subject to electronic predissociation.^{26,27} Other aspects of the conversion from saturated LIF intensities to populations are unchanged from prior studies.^{28,29}

The improved procedures take into account the transmission of the bandpass filter $T(\lambda_i)$ at the emission wavelengths (λ_i) from a particular upper state, OH $A^2\Sigma^+$ (ν', N', F'). The fraction of the emission that is transmitted through the bandpass filter $T(\nu', N', F')$, is given by

$$T(\nu', N', F') = \frac{\sum_i T(\lambda_i) A_i}{\sum_i A_i}.$$

The summation index spans over the allowed transitions from the upper state, $i \equiv A^2\Sigma^+(\nu', N', F') \rightarrow X^2\Pi(\nu'', J''_{OH}, \Omega'', \Lambda'')$. The quantum labels ν' , N' , and F' refer to vibration, rotation (neglecting spin), and spin-rotation components of the excited OH $A^2\Sigma^+$ electronic state.^{24,30} In general, for a specific ν' , N' level in the $A^2\Sigma^+$ state, there are six emission lines associated with each $A-X(\nu', \nu'')$ vibronic transition. The emission coefficients A_i associated with these transitions include Franck-Condon and Hönl-London factors.²⁵

In addition, the improved analysis accounts for the total lifetime τ , in this case arising from radiative decay and/or predissociation, as well as the fluorescence quantum yield $\Phi_f(\nu', N', F')$ of the OH $A^2\Sigma^+$ emitting state. The total lifetime affects the fraction of the fluorescence decay collected during integration of a boxcar gate running from time t_1 to t_2 ,

$$G(\tau, t_1, t_2) = e^{-t_1/\tau} - e^{-t_2/\tau}.$$

The intensity of fluorescence I_f detected from a particular OH $A^2\Sigma^+$ (ν', N', F') state is given by

$$I_f \propto G(\tau, t_1, t_2) \Phi_f(\nu', N', F') T(\nu', N', F'),$$

with the proportionality sign used to indicate other experimental factors that are unchanged for different upper states, such as the fraction of light impinging on the collection optics and the PMT detection efficiency.

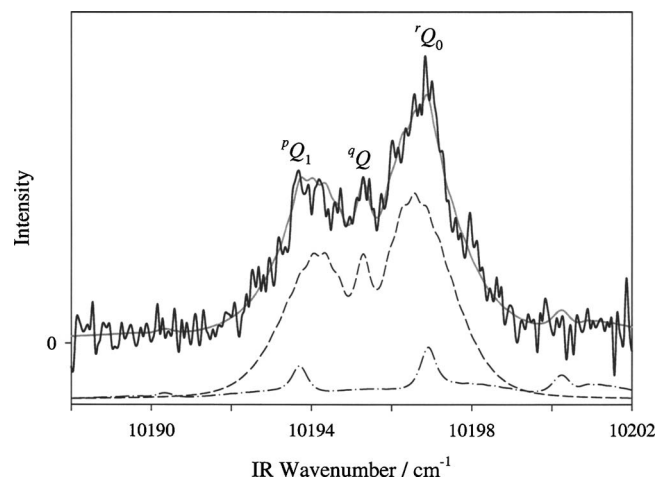


FIG. 2. Infrared action spectrum of the second OH overtone transition of tp-HOONO at $10\,195.32(5)\text{ cm}^{-1}$ (origin), recorded with the UV probe laser fixed on the OH A-X (1,0) $Q_1(9/2)$ transition. The simulation of the rotational band contour (solid line) is generated from the rotational constants derived from a fit to the first OH overtone band. A least-squares fit of the intensity profile yielded a hybrid band type of $a:c=4.2(7):1$, rotational temperature of $5.2(2)\text{ K}$, and a homogeneous linewidth of $0.44(12)\text{ cm}^{-1}$. The a -type (dashed line) and c -type (dot-dashed line) components of the simulation are also shown.

III. RESULTS AND ANALYSIS

A. OH overtone excitation of tp-HOONO

1. Experimental spectrum and simulation

The infrared action spectrum of tp-HOONO in the second OH overtone region is observed at $10\,195.32(5)\text{ cm}^{-1}$ (origin) under jet-cooled conditions. The action spectrum shown in Fig. 2 is obtained by scanning the IR laser with the UV laser detecting OH ($\nu=0$, $J_{\text{OH}}=9/2$) fragments on the A-X(1,0) $Q_1(9/2)$ transition. This OH product channel yields the largest IR-induced signal (S) relative to background (B) from unreacted OH in the jet ($S/B \sim 1/2$). The spectrum displayed in Fig. 2 is the sum of four scans, with each point resulting from 600 IR laser shots. The second OH overtone transition of tp-HOONO is identified by its vibrational frequency and rotational band contour.

A Birge-Sponer plot has been constructed using the second OH overtone ($10\,195.3\text{ cm}^{-1}$) and the previously reported first overtone (6971.4 cm^{-1}) (Refs. 11 and 22) transitions of tp-HOONO in Fig. 3. The local mode behavior of the OH stretching mode of tp-HOONO is similar to that found for nitric acid^{31–35} and the OH radical itself,³⁶ which are also displayed in Fig. 3. The harmonic frequency $\omega_e = 3747.5\text{ cm}^{-1}$ and anharmonicity $\omega_e x_e = 87.3\text{ cm}^{-1}$ for tp-HOONO are readily extracted from the Birge-Sponer plot. By contrast, the considerably lower OH stretch frequency ($\omega_e = 3553.0\text{ cm}^{-1}$) and increased anharmonicity ($\omega_e x_e = 123.5\text{ cm}^{-1}$) of cc-HOONO,^{10,13} arising from its intramolecular hydrogen bond, distinguish its local mode behavior from the other species.

In addition, the rotational band contour of the second OH overtone transition of tp-HOONO (Fig. 2) closely resembles that of the first overtone transition.^{11,22} In both cases, the band contour is that of a near-prolate asymmetric top with prominent contributions from both a - and c -type

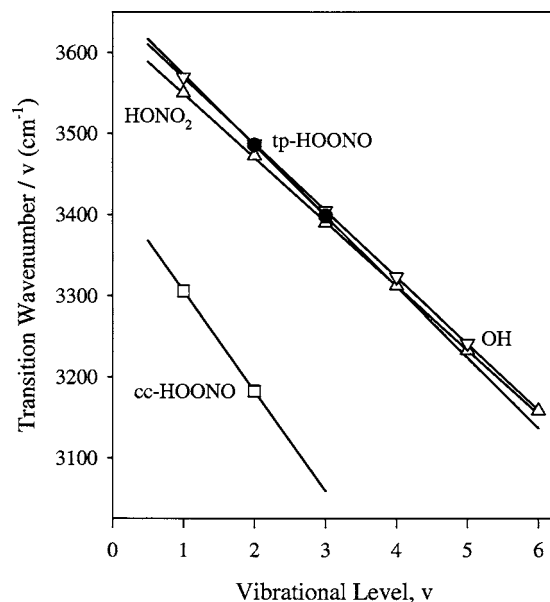


FIG. 3. Birge-Sponer plot for the OH stretching modes of tp-HOONO (filled circles), HONO₂ (up triangles), and the OH radical (down triangles), showing the similarity of their local mode behavior. The cc-HOONO conformer (squares) is distinctly different due to its intramolecular hydrogen bond. The OH stretch transition frequencies are taken from this laboratory's work (Refs. 11 and 22) for tp-HOONO and Refs. 10, 13, and 31–36 for the other species.

transitions (and negligible b -type component). The qQ branch of the a -type (parallel) transition at $10\,195.3\text{ cm}^{-1}$ gives rise to the peak in the central region of the band, while the c -type (perpendicular) transition Q branches, pQ_1 at $10\,193.7\text{ cm}^{-1}$ and rQ_0 at $10\,196.9\text{ cm}^{-1}$, contribute to the peaks at the edges of the band (along with the P and R branches of the a -type transition). The Q -branch labels refer to ΔK_a (superscript) and K_a'' (subscript) in the prolate symmetric top limit.

A simulation generated using the rotational constants derived for the ground and upper ($2\nu_{\text{OH}}$) vibrational states from the first OH overtone transition of tp-HOONO (Ref. 11) is superimposed on the experimental data for the second overtone transition in Fig. 2. The a - and c -type components of the simulation are also shown in Fig. 2. The remarkable agreement identifies the band at $10\,195.3\text{ cm}^{-1}$ as originating from tp-HOONO. There is no observable change in the rotational constants for tp-HOONO ($3\nu_{\text{OH}}$) as compared with $2\nu_{\text{OH}}$ at the level of detail that can be extracted from the experimental spectrum. Indeed, the rotational constants previously derived from the first overtone transition had already indicated minimal structural change in tp-HOONO upon vibrational excitation of the OH stretching mode.¹¹

The spectral simulation also depends on several other parameters, namely, the Lorentzian linewidth, rotational temperature, and the a - to c -type transition ratio. These parameters are determined in a least-squares fitting procedure to match the intensity profile and linewidth of the experimental spectrum. Although all three of these parameters are sensitive to even partial saturation in the spectrum, this effect is expected to be negligible for the second OH overtone transition because of its weak oscillator strength (see below). Nevertheless, there is substantial homogeneous line broaden-

ing from some other source that is much greater than the OPO bandwidth of 0.12 cm^{-1} . The best fit results in a rotational temperature of $5.2(2)\text{ K}$, a Lorentzian linewidth of $0.44(12)\text{ cm}^{-1}$, and an $a:c$ ratio of $4.2(7):1$. The uncertainties (1σ) reflect the significant correlation between the fitted parameters. The $a:c$ ratio is considerably different than the $1.2(1):1$ ratio observed for the first OH overtone transition,¹¹ indicating a change in the direction of the transition dipole moment with increasing OH stretch excitation (see next section). The apparent linewidth is about a factor of two times larger than seen for the first overtone transition where $\Gamma=0.195(4)\text{ cm}^{-1}$.¹¹ As will be discussed later, the homogeneous line broadening is attributed to intramolecular vibrational redistribution (IVR).¹¹ A direct measurement of the tp-HOONO ($3\nu_{\text{OH}}$) dissociation lifetime in the time domain is precluded by the laser pulse width (6 ns).

2. Transition dipole moment

The second OH overtone transition of tp-HOONO is observed to be a hybrid band with a $4.2(7):1$ ratio of the $a-$ to $c-$ type components of the transition moment. This $a:c$ ratio indicates that the transition dipole lies 49° off of the OH bond axis. In contrast, the $a:c$ ratio determined for the first overtone transition of $1.2(1):1$ reveals that the transition dipole points 35° off of the OH bond axis. The 14° change in the direction of the transition dipole moment results in more than a threefold change in the $a:c$ intensity ratio due to trigonometric considerations. In both cases, the result is significantly different from the bond dipole approximation,³⁷ which assumes that the transition dipole lies along the OH bond axis and would give rise to a 1 to 12 ratio of the $a-$ to $c-$ type components. The orientation of the transition dipole moment for the OH overtone transitions presumably reflects changes in the charge distribution of the tp-HOONO molecule upon OH stretch excitation.³⁸

The relative oscillator strength for the first and second OH overtone transitions of tp-HOONO has also been determined by comparing the signal intensities of the strongest peak in each IR spectrum while probing the OH products on the $A-X(1,0) Q_1(9/2)$ line. The IR pump beam at 0.98 or $1.4\ \mu\text{m}$ was carefully aligned with the UV probe beam, which was unchanged while switching between the IR sources. For these measurements, the UV beam was kept slightly larger than either IR beam. Next, spectral simulations were used to convert the measured intensity of the strongest peak in each IR spectrum to the integrated intensity of the vibrational band. The integrated band intensities were then changed to relative oscillator strength by taking into account the photon flux (pulse power divided by transition frequency). Finally, the fraction of OH products in the specified product state, $\nu=0, J_{\text{OH}}=9/2, \Omega=3/2, \Pi(A'')$, was obtained from the statistical calculations for dissociation of tp-HOONO ($3\nu_{\text{OH}}$) and ($2\nu_{\text{OH}}$),³⁹ since the OH products are spread over many more internal energy states for $3\nu_{\text{OH}}$ than $2\nu_{\text{OH}}$. The net result is that the oscillator strength for the second OH overtone transition of tp-HOONO is found to be ~ 14 times weaker than that for the first overtone transition. This ratio neglects the unobserved HO_2+NO product channel for tp-HOONO ($3\nu_{\text{OH}}$).⁴⁰

B. OH product state distribution

1. Experimental rotational distribution

Information about the unimolecular decay dynamics of tp-HOONO ($3\nu_{\text{OH}}$) is obtained from the nascent quantum state distribution of the OH ($\nu=0$) and ($\nu=1$) products. For these experiments, the infrared laser is fixed on the most intense peak in the tp-HOONO second OH overtone spectrum at $10\ 196.9\text{ cm}^{-1}$, while the UV laser is tuned to various lines of the OH $A-X(1,0)$ and $(0,1)$ transitions to determine the relative population of the OH products in each internal energy state. The excess energy available for internal excitation and/or translational recoil of the OH+NO₂ products is obtained by subtracting the previously determined binding energy for tp-HOONO $D_0=5667(38)\text{ cm}^{-1}$ (Ref. 11) from the photon energy, yielding $E_{\text{avail}}=4530(38)\text{ cm}^{-1}$.

As shown in Fig. 4, the OH ($\nu=0$) product state distribution resulting from $3\nu_{\text{OH}}$ excitation peaks at low rotational states in each spin-orbit (Ω) manifold, $J_{\text{OH}}=7/2$ (or $9/2$), $\Omega=3/2$, and $J_{\text{OH}}=9/2, \Omega=1/2$ with internal energies $E_{\text{OH}}=202$ (or $355)\text{ cm}^{-1}$ and $E_{\text{OH}}=608\text{ cm}^{-1}$, respectively, and falls off smoothly with increasing rotational excitation (J_{OH}). One of the most populated states, $J_{\text{OH}}=9/2, \Omega=3/2, \Pi(A'')$, served as a reference channel. The OH ($\nu=0, J_{\text{OH}}$) distribution appears to extend to the energetic limit of $4530(38)\text{ cm}^{-1}$ in both spin-orbit manifolds. The highest J_{OH} levels are probed on OH $A-X(1,0)$ transitions that access predissociative rotational levels ($N' > 13$) of the OH $A^2\Sigma^+$ ($\nu'=1$) state.^{26,27} The improved analysis procedures (Sec. II) take into account the total lifetime and fluorescence quantum yield of the emitting state.²⁵ The observed OH ($\nu=0$) population distribution could not be normalized because a few transitions could not be measured. Instead, a normalization constant was chosen that gives the best agreement with all three statistical models (Fig. 4). The OH ($\nu=0$) product state distribution appears to be statistical with no lambda-doublet (Λ) or spin-orbit (Ω) propensities, as will be demonstrated in the next section when the experimental distribution is compared with several statistical models.

Significantly less population is detected for vibrationally excited OH ($\nu=1$) products. These products contain 3568.5 cm^{-1} of vibrational energy, leaving at most $962(38)\text{ cm}^{-1}$ available for rotational and/or spin-orbit excitation of the OH fragment. In this case, the most populated $J_{\text{OH}}=5/2, \Omega=3/2, \Pi(A'')$ state with $E_{\text{OH}}=3649\text{ cm}^{-1}$ served as the reference channel. The population in this product channel is approximately 30 times smaller than that found for the OH ($\nu=0$) reference channel, as elaborated below. Such small populations naturally have relatively large uncertainties associated with them. As a result, we were not able to obtain a meaningful product rotational distribution for OH ($\nu=1$). Instead, we focused on a careful measurement of the relative population of the reference channel for $\nu=1$ compared with that for $\nu=0$. This provides an important benchmark for testing various statistical theories.

Also shown in Fig. 4 is the OH ($\nu=0$) product state distribution observed following dissociation of tp-HOONO ($2\nu_{\text{OH}}$), which is reproduced from Ref. 11. The same statistical models are applied to this unimolecular decay process,

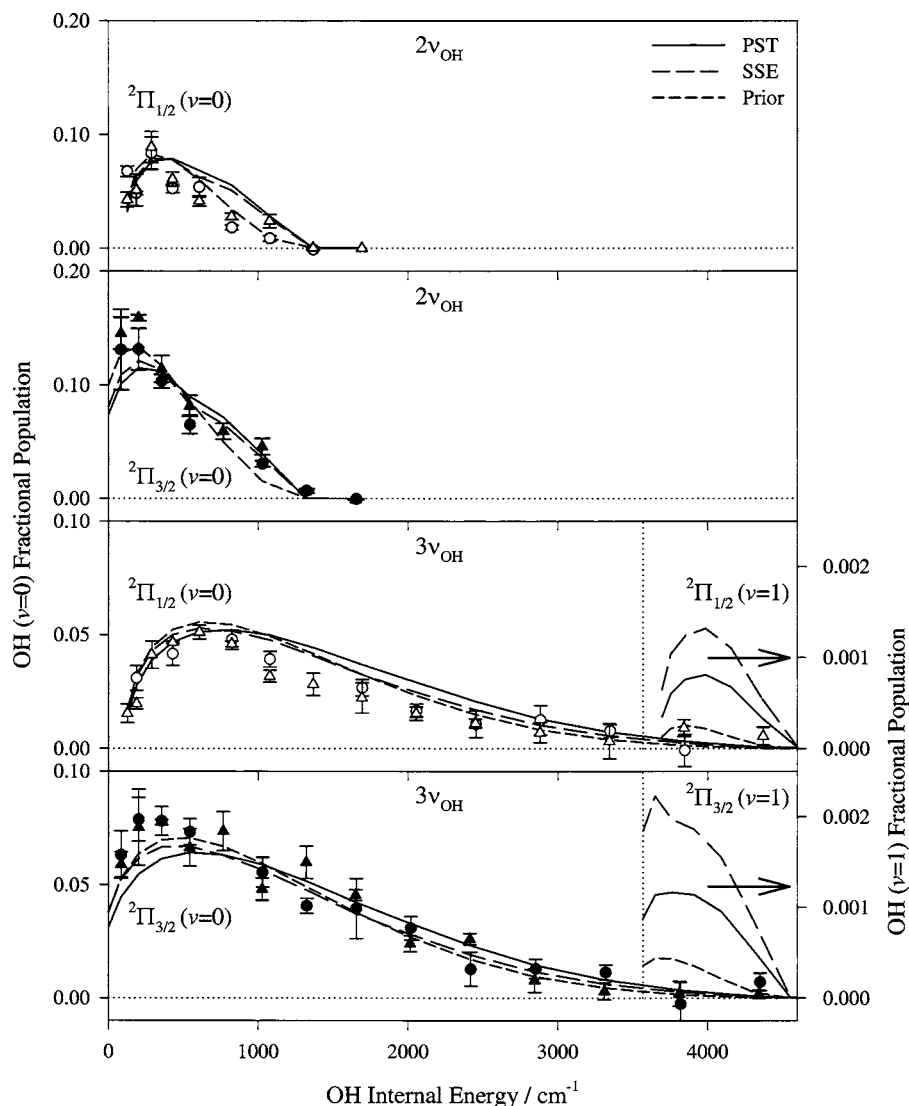


FIG. 4. Internal energy distribution of the OH ($\nu=0$, J_{OH}) products observed in the excited ${}^2\Pi_{1/2}$ (open symbols) and ground ${}^2\Pi_{3/2}$ (filled symbols) spin-orbit manifolds following dissociation of tp-HOONO ($2\nu_{\text{OH}}$), top panels (from Ref. 11), and ($3\nu_{\text{OH}}$), bottom panels. The $\Pi(A'')$ and $\Pi(A')$ Λ -doublet components are distinguished by circle and triangle symbols, respectively. The smooth curves through the experimental data are obtained from three different statistical models, namely, a prior distribution (prior), phase-space theory (PST), and the separate statistical ensembles (SSE) model. For tp-HOONO ($3\nu_{\text{OH}}$), the three statistical models predict extremely small OH ($\nu=1$, J_{OH}) populations (enhanced 40 \times and referenced to the right axis) in the two spin-orbit manifolds.

extending our previous investigation of this process. In this case E_{avail} is 1304(38) cm^{-1} , as determined from a fit to a microcanonical statistical distribution constrained only by the energy available to the products (prior distribution).¹¹ An equivalent available energy is obtained from the highest observed OH product state, $J_{\text{OH}}=17/2$, $\Omega=3/2$, with $E_{\text{OH}}=1324.3 \text{ cm}^{-1}$.¹¹

2. Vibrational branching ratio

The relative LIF intensities of the OH A-X lines used to probe the $\nu=0$ and $\nu=1$ reference channels following dissociation of tp-HOONO ($3\nu_{\text{OH}}$), namely, OH A-X(1,0) $Q_1(9/2)$ and (0,1) $Q_1(5/2)$ lines, were carefully measured under similar experimental conditions. Converting these intensities into relative populations requires a detailed analysis since different vibronic transitions were utilized. In addition, several experimental parameters had to be changed, most importantly the bandpass filter used for collecting fluorescence.

The LIF intensity data was recorded with $\sim 1 \text{ mJ/cm}^2$ per pulse of UV radiation in both cases, which is more than enough to saturate the OH A-X(1,0) $Q_1(9/2)$ and (0,1) $Q_1(5/2)$ transitions. As a result, it is not necessary to

include their relative transition probabilities in the analysis that follows. Instead, one can assume in each case that half of the population in the lower state is transferred to the upper state.

On the other hand, the fluorescence emission from the upper states of these transitions, OH A ${}^2\Sigma^+$ ($\nu'=1$, $N'=4$) and ($\nu'=0$, $N'=2$), is detected with different efficiencies, and this must be taken into account (see Sec. II). The bandpass filters were selected to transmit emission primarily from diagonal transitions OH A-X (1,1) or (0,0) at 315 or 309 nm, respectively. These filters have somewhat different transmission properties at the relevant wavelengths. In addition, the upper states of the reference lines have slightly different lifetimes, but neither are subject to electronic predissociation and both have unit fluorescence quantum yields.²⁵

The relative LIF intensities for the OH A-X(1,0) $Q_1(9/2)$ and (0,1) $Q_1(5/2)$ lines were measured following second OH overtone excitation of tp-HOONO, and converted to relative population of the OH X ${}^2\Pi_{3/2}$ ($\nu=0$, $J_{\text{OH}}=9/2$) and ($\nu=1$, $J_{\text{OH}}=5/2$) levels using the procedure outlined above. A ratio of ~ 0.037 is obtained for the relative population in the $\nu=1$ to $\nu=0$ reference channels.

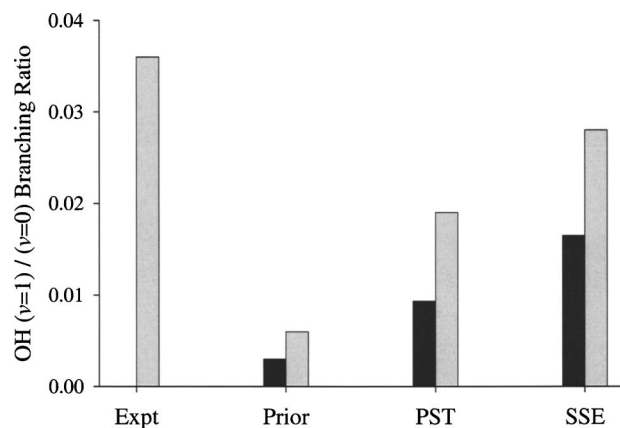


FIG. 5. Vibrational branching ratio for OH ($\nu=1$) to ($\nu=0$) products from the experiment and various statistical models following dissociation of tp-HOONO ($3\nu_{\text{OH}}$). The gray bars are the experimental measurement and model predictions for the relative population of the reference channels, namely, OH ($\nu=1$, $J_{\text{OH}}=5/2$, $\Omega=3/2$) and OH ($\nu=0$, $J_{\text{OH}}=9/2$, $\Omega=3/2$). The black bars are the statistical model predictions for the OH ($\nu=1$) to ($\nu=0$) ratio after summing over product rotational and fine-structure states.

This ratio is plotted as a bar graph in Fig. 5 and compared with the results of various statistical models in the next section.

IV. STATISTICAL MODELS FOR tp-HOONO DISSOCIATION

A. Statistical model formulation

In a previous publication on the unimolecular decay dynamics of tp-HOONO ($2\nu_{\text{OH}}$),¹¹ we compared the distribution of OH ($\nu=0$) fragments over rotational and spin-orbit states to the predictions of a prior distribution,^{41,42} and found excellent agreement. We now extend our examination of statistical models for dissociation of tp-HOONO by considering both phase-space theory (PST) and the separate statistical ensembles (SSE) model.^{43,44} In this new work, we apply the latter two models to the previously reported OH fragment distributions that result from excitation of the first OH overtone in tp-HOONO and all three models to the fragments that result from second overtone excitation. In the calculations, we specifically take into account the quantized nature of the OH and NO₂ vibrations and rotations, but treat the relative translational energy as a classical function. The energies of the OH rotational states for both vibrational levels ($\nu=0, 1$) and both spin-orbit states ($\Omega=1/2, 3/2$) are taken from the work of Dieke and Crosswhite.²⁴ We treat the NO₂ fragment as an anharmonic oscillator, using the vibrational constants of Bist and Brand.⁴⁵ As a near-prolate symmetric top ($\kappa=-0.994$), we model the NO₂ rotations with symmetric top energy levels, invoking ¹⁶O nuclear-spin statistics to eliminate the degeneracy of rotational levels with $K>0$ and exclude levels for which $K=0$ and $J=\text{odd}$.

In the prior distribution, the OH product states are assumed to be populated with equal probability, subject only to an energy constraint.^{41,42} The probability of populating specific OH ($\nu, J_{\text{OH}}, \alpha_{\text{OH}}$) and NO₂ ($\nu_{\text{NO}_2}, J_{\text{NO}_2}, \alpha_{\text{NO}_2}$) product states at a given total energy is represented by

$$P(\nu, J_{\text{OH}}, \alpha_{\text{OH}}, \nu_{\text{NO}_2}, J_{\text{NO}_2}, \alpha_{\text{NO}_2} | E_{\text{avail}}) = C(2J_{\text{OH}} + 1)(2J_{\text{NO}_2} + 1)E_t^{1/2},$$

with

$$E_t = E_{\text{avail}} - E_{\text{OH}} - E_{\text{NO}_2}.$$

Here, $(2J_{\text{OH}}+1)$ is the degeneracy of OH rotational states, $(2J_{\text{NO}_2}+1)$ is the degeneracy of NO₂ rotational states, and $E_t^{1/2}$ is the density of translational states associated with the relative motion of the separating OH and NO₂ fragments. The factor C is simply a normalization constant. The index ν is the OH vibrational quantum number and α_{OH} refers to the additional quantum labels that are needed to characterize the OH fragment, namely, its spin-orbit (Ω) and lambda-doublet (Λ) state. Similarly, the index α_{NO_2} is used to account for the relevant quantum numbers of the NO₂ symmetric top N_{NO_2} and K_{NO_2} . The quantum number ν_{NO_2} refers to the vibrational degrees of freedom of the NO₂ fragment. The vertical line separating E_{avail} from other parameters indicates that the available energy is a constraint on the distribution. In the experiment, we examine the probability of the OH products being formed in a given quantum state ($\nu, J_{\text{OH}}, \alpha_{\text{OH}}$). As a result, we sum the prior distribution given above over the unobserved NO₂ rotational and/or vibrational states. The resulting OH distribution is given by

$$P(\nu, J_{\text{OH}}, \alpha_{\text{OH}} | E_{\text{avail}}) = C(2J_{\text{OH}} + 1) \sum_{\nu_{\text{NO}_2}, J_{\text{NO}_2}, \alpha_{\text{NO}_2}} (2J_{\text{NO}_2} + 1)E_t^{1/2}.$$

In the PST calculations,^{34,42,43} we apply the additional constraint that the total angular momentum of the system must be conserved. PST also differs from a prior distribution in the treatment of the translational density of states, as documented in the literature.⁴³ The conservation of total angular momentum results in a significant decrease in the number of states that can be populated. Specifically, we assume throughout the calculations that $J=4$, which is the approximate mean of the HOONO rotational states comprising the rQ_0 branch and populated at 3–5 K in the free jet expansion. (The calculated fragment distributions are nearly the same for total $J=0-10$, a range that encompasses more than 95% of the tp-HOONO molecules excited on the rQ_0 branch.) The total angular momentum \mathbf{J} is the vector sum of the fragment angular momenta and the orbital angular momentum of the recoiling fragments \mathbf{L} ,

$$\mathbf{J} = \mathbf{J}_{\text{OH}} + \mathbf{J}_{\text{NO}_2} + \mathbf{L}.$$

In the PST calculations, we sum over \mathbf{L} and all of the energetically accessible NO₂ states for each OH rotational state, subject to the conservation of angular momentum. We further restrict the possible values of the orbital angular momentum by calculating the height of the centrifugal barrier that arises from modeling the OH–NO₂ attraction as a simple $1/R^6$ interaction, where R is the center-of-mass distance between the OH and NO₂ fragments. In this case, the height of the centrifugal barrier V_{max} is given by

$$V_{\max} = \frac{[L(L+1)]^{3/2} \hbar^3}{3\sqrt{6} \mu^{3/2} C_6^{1/2}}.$$

We have adopted the value of the C_6 coefficient that was found by Sinha *et al.*³⁴ to reproduce the OH product state distribution that results from overtone-induced dissociation of nitric acid at 300 K. (Our PST calculations are insensitive to this value, presumably because the restriction to a low value of total J reduces the range of possible values of the orbital angular momentum and thus the importance of the centrifugal barrier in moderating the dissociation dynamics.) The state count corresponding to a particular OH state ($\nu, J_{\text{OH}}, \alpha_{\text{OH}}$) excludes any set of values of ($\nu_{\text{NO}_2}, J_{\text{NO}_2}, \alpha_{\text{NO}_2}$) with available energy that is insufficient to surmount the centrifugal barrier.

We have also considered the predictions of phase-space theory in assessing the importance of the competing NO + HO₂ dissociation channel following $3\nu_{\text{OH}}$ excitation.⁴⁶ For this calculation, we have considered HO₂ to be a prolate symmetric top ($\kappa = -0.994$),⁴⁷ though in this case there are no nuclear-spin restrictions on the allowed rotational states. We also utilize the known vibrational fundamental frequencies of HO₂ and the well-determined rotational constants of NO.^{48,49}

The SSE approach to unimolecular dissociation is a variant on phase-space theory proposed initially by Wittig *et al.*⁴⁴ to account for the frequent observation that phase-space theory *underestimates* the degree of fragment vibrational excitation while *overestimating* the fragment rotational excitation. In this approach, the vibrational distributions in the products are determined by considering a restricted region of phase space that corresponds only to the vibrational degrees of freedom that have “disappeared” along the dissociation reaction coordinate. This is equivalent to assuming that the rotational degrees of freedom of the parent do not contribute to the density of states that determines the product vibrational distribution. For the case of HOONO dissociating to OH + NO₂, the parent has nine vibrational degrees of freedom and three rotational degrees of freedom. In the products, there are four vibrational and five rotational degrees of freedom, along with three translational degrees of freedom. In a phase-space theory calculation of, for example, the NO₂ vibrational distribution, we count the number of energetically accessible states, subject to the conservation of energy and the limitations imposed by the centrifugal barrier. In the classical (high-energy) limit, the density of rotational and translational states for this set of fragments (and $J \rightarrow 0$) will vary as $(E_{\text{avail}} - E_{\text{vib}})^2$, where E_{avail} is the energy available for disposal into the fragment internal and/or translational degrees of freedom and E_{vib} is the NO₂ vibrational energy. In a SSE calculation, it is only the five “disappearing” vibrational degrees of freedom that contribute to the fragment vibrational distribution. This five-dimensional density-of-states function varies more slowly, as $(E_{\text{avail}} - E_{\text{vib}})^{3/2}$. Thus excited fragment vibrational states will have higher population than in a phase-space theory calculation. By conservation of energy, the corresponding fragment rotational degrees of freedom must contain a smaller fraction of the available energy.

B. Statistical model predictions

The three statistical models (PST, SSE, and prior) predict remarkably similar OH ($\nu=0$) product state distributions following first OH overtone excitation and also similar distributions following second OH overtone excitation of tp-HOONO as shown in Fig. 4. For both $2\nu_{\text{OH}}$ and $3\nu_{\text{OH}}$ excitations, the calculated distributions exhibit a trend of increasing population with rotational excitation at low J_{OH} that can be attributed to the increasing degeneracy of the rotational states. The population distributions then follow a rapid decrease (for $2\nu_{\text{OH}}$) or a more gradual decrease (for $3\nu_{\text{OH}}$) with increasing rotational excitation as energy restrictions, $E_{\text{avail}} = 1304 \text{ cm}^{-1}$ (for $2\nu_{\text{OH}}$) and 4530 cm^{-1} (for $3\nu_{\text{OH}}$), overtake the degeneracy factor. The angular momentum constraint associated with the PST and SSE models does not appreciably affect the product state distribution or its fall off at high J_{OH} . The two spin-orbit states follow the same population distribution after accounting for the degeneracy of the states, and the two Λ -doublet components of each rotational level have similar populations. The PST calculations by Matthews and Sinha for tp-HOONO ($2\nu_{\text{OH}}$) shown in Fig. 6 of Ref. 12 differ slightly from the present work in that they average over a thermal (300 K) distribution of initial HOONO states, rather than the limited HOONO rotational states populated at 3–5 K.

All the three statistical models indicate that vibrationally excited OH is a very minor channel in the dissociation of tp-HOONO ($3\nu_{\text{OH}}$) with less than 2% of the OH products formed in $\nu=1$. However, the models differ in the fractional populations in OH ($\nu=1$) (Fig. 4, note the $40\times$ magnification) as well as the OH ($\nu=1$)/($\nu=0$) product branching ratios (Fig. 5). As expected from the formulation,⁴⁴ the SSE model predicts the largest fractional population for OH ($\nu=1$) and product branching ratio, followed by PST and then the prior distribution. The rotational distribution for the OH ($\nu=1$) products peaks at low J_{OH} and then falls off rapidly due to the very limited energy available for rotational and/or spin-orbit excitation (962 cm^{-1}). For very low J_{OH} only, the NO₂ product can be released with bending excitation (742 cm^{-1}), creating a small bump in the calculated product state distribution.

Interestingly, the unobserved HO₂+NO product channel is predicted to be significant upon the dissociation of tp-HOONO ($3\nu_{\text{OH}}$) with 21.5% of the total products. The statistical calculations (PST) indicate that the lower energy OH+NO₂ channel will be favored over the higher energy HO₂+NO channel ($+7.5 \text{ kcal mol}^{-1}$) by a factor of 3.66. This suggests alternate detection schemes for HOONO using action spectroscopy.

C. Comparison of results from experiment and statistical models

In general, the experimental OH ($\nu=0$) product state distributions observed following first and second OH overtone excitation of tp-HOONO can be termed “statistical,” since there is very good agreement with the statistical models (Fig. 4).¹¹ However, there are noticeable differences; specifically, the experimental distributions appear to be rotationally

colder particularly at low J_{OH} than the predictions of all three statistical models. The origin of this discrepancy is not known. It cannot be attributed to the neglect of angular momentum conservation in the prior model,^{41,42} since this constraint is explicitly included in the PST and SSE models.^{43,44} While it has been previously noted that PST tends to favor rotational over vibrational excitation of products in unimolecular dissociation processes, the SSE model was developed to address this issue,⁴⁴ yet it does not give better agreement with the experimental data at low J_{OH} .

The vibrational distribution of the OH products from tp-HOONO ($3\nu_{\text{OH}}$) provides a more stringent test of the three statistical models. However, the OH ($\nu=1$) products are such a minor channel that we were unable to quantitatively determine the branching ratio summed over all the OH product rotational and fine-structure states. Instead, we measured a specific quantum state ratio for OH $X^2\Pi_{3/2}$, ($\nu=1, J_{\text{OH}}=5/2$)/($\nu=0, J_{\text{OH}}=9/2$), and compared this result with the analogous ratios from the three statistical models in Fig. 5 (gray bars). The SSE model prediction matches the experimental observation (~ 0.037) most closely with a ratio of 0.028. Both the PST and prior models predict even smaller quantum state ratios.

V. DISCUSSION

The second OH overtone transition of tp-HOONO has been definitively identified at $10\,195.32(5)\text{ cm}^{-1}$ (origin) through its vibrational frequency and rotational band structure under jet-cooled conditions (5 K). The observed transition frequency is in excellent accord with theoretical predictions. Varner and Stanton predicted a transition frequency of $10\,191\text{ cm}^{-1}$ using the CCSD(T) level of *ab initio* theory with the atomic natural orbital (ANO) basis set⁵⁰ in conjunction with second-order vibrational perturbation theory.^{11,51} In addition, Matthews *et al.* predicted the same value in their scaled *ab initio* transition frequency calculations.²⁰ The prominent feature at $10\,160\text{ cm}^{-1}$ in the room-temperature spectrum reported by these same authors, however, cannot be attributed to tp-HOONO ($3\nu_{\text{OH}}$), as previously suggested.²⁰ Spectral simulations based on the parameters derived in this work show that the band position at 300 K will not shift appreciably from the reported band origin. The prominent feature in the second OH overtone spectrum at 300 K (Ref. 20) is most likely due to hot bands originating from excited torsional states of cc-HOONO, as recently reported for the first and second OH overtone transitions.^{12,15,16}

Konen *et al.* have also computed the magnitude and direction of the transition dipole moment for the OH overtone transitions of tp-HOONO.¹¹ Several different types of calculations were performed, which were based on second-order vibrational perturbation theory (VPT2) in full dimensionality [nine dimensional (9D)] and reduced dimensionality [one dimensional (1D)], and an exact 1D calculation.¹¹ For the second overtone transition of tp-HOONO, the full dimensionality VPT2 calculation yields a ratio of 3.48:1 for the *a*- to *c*-type transition intensities, which is in good accord with the experimental ratio of 4.2(7):1 determined in this work. The reduced dimensionality VPT2 calculation gives a similar ra-

tio of 3.44:1, while the exact 1D calculation predicts a smaller *a*:*c* ratio of 2.30:1. By comparison, the VPT2-9D calculation for the first overtone transition of tp-HOONO gives an *a*:*c* ratio of 1.38:1, which is also in good agreement with the experimental ratio of 1.2(1):1.¹¹ Reduced dimensionality calculations yield similar *a*:*c* ratios of 1.36 (VPT2) and 1.22 (exact 1D). Both experiment and theory show that the direction of the transition dipole moment, as evidenced by the *a*:*c* ratio, changes with increasing OH stretch excitation. The transition dipole shifts from approximately 35° to 49° with respect to the OH bond axis (in the *a*-*c* plane) from the first to second OH overtone transition. This reflects changes in the charge distribution of the tp-HOONO molecule upon OH stretch excitation.³⁸

Konen *et al.*¹¹ and Varner and Stanton⁵¹ predicted the oscillator strength for the first OH overtone transition of tp-HOONO to be 1.04×10^{-6} and that for the second overtone transition to be 4.82×10^{-8} , indicating that the latter is ~ 21 times weaker. Matthews *et al.* predicted a similar 24-fold decrease in the integrated absorption cross section for the second OH overtone of tp-HOONO as compared with the first overtone at their highest level of theory.²⁰ Experimentally, we estimate that the second overtone is about 14 times weaker than the first overtone of tp-HOONO.

The Lorentzian linewidth of $\Gamma=0.44(12)\text{ cm}^{-1}$ observed for the second OH overtone transition is about a factor of two times larger than that for the first overtone transition, $\Gamma=0.195(4)\text{ cm}^{-1}$.¹¹ The corresponding lifetime of 12 ps for tp-HOONO ($3\nu_{\text{OH}}$) is attributed to IVR by analogy with the arguments used to explain the $2\nu_{\text{OH}}$ lifetime of 27(1) ps.¹¹ The factor of two change in lifetime and/or linewidth, however, is much smaller than might be predicted using Fermi's golden rule based on the change in the density of states (and an assumed constant average coupling strength). An anharmonic frequency state count yields a density of states increasing 7.5-fold from 120 states per cm^{-1} at $2\nu_{\text{OH}}$ to 900 states per cm^{-1} at $3\nu_{\text{OH}}$.⁵²⁻⁵⁴ This suggests that the optically bright OH stretch is coupled strongly to only a small subset of vibrational states (first tier), and that most of the states in the count are more weakly coupled background states. Thus, the experimental linewidth measurements are consistent with a tier model for IVR.⁵⁵⁻⁵⁷

The statistical OH product state distributions observed following $2\nu_{\text{OH}}$ and $3\nu_{\text{OH}}$ excitation of tp-HOONO indicate some degree of energy randomization prior to dissociation, which occurs faster than the temporal resolution of our lasers (6–8 ns). The tp-HOONO dissociation rates are much slower than predicted by the Rice-Ramsperger-Kassel-Marcus theory (≤ 1 ps),¹¹ presumably because the coupling of the high-frequency OH stretch to other states is a rate-limiting step in the dissociation process. In addition, the observed statistical distributions provide no evidence of a barrier ($\sim 4.5\text{ kcal mol}^{-1}$) to dissociation of tp-HOONO, which is evident in theoretical calculations.^{58,59} This suggests that dissociation of tp-HOONO ($2\nu_{\text{OH}}$ and $3\nu_{\text{OH}}$) may involve isomerization to the cc-HOONO conformer followed by barrierless dissociation.⁵⁸ The initial OH overtone excitation prepares tp-HOONO far above the conformational barrier separating tp- from cc-HOONO.¹³

Finally, we have not yet seen any spectroscopic evidence for *cc*-HOONO in jet-cooled spectra in the first or second OH overtone region, despite significant effort in spectroscopic searches. We have previously rationalized our inability to observe the first OH overtone transition of *cc*-HOONO, reported at 6365 cm^{-1} under thermal conditions, as resulting from the increased binding energy of the *cc*-HOONO conformer ($19.6\text{ kcal mol}^{-1}$).¹¹ This binding energy would imply that only spectral features with transition frequencies greater than 6860 cm^{-1} should be observable by infrared action spectroscopy under jet-cooled conditions.

On the other hand, the second overtone transition will supply more than sufficient energy for the dissociation of *cc*-HOONO. Thus, our inability to observe *cc*-HOONO ($3\nu_{\text{OH}}$) under jet-cooled conditions likely arises from (1) inadequate transition strength or other related factors that make *cc*-HOONO more difficult to observe spectroscopically or (2) insufficient production of the more stable *cc*-HOONO conformer in our photolytic source. The latter can be overcome by switching to an alternate synthetic route for the production of *cc*-HOONO from $\text{H}_2\text{O}_2 + \text{BF}_4\text{NO}$,^{12,13,21} which is in progress. The former could arise from the twofold weaker transition strength computed for the second OH overtone of *cc*-HOONO compared with *tp*-HOONO^{20,51} or perhaps additional line broadening (reducing the peak amplitude) due to faster IVR for this conformer.¹³ We estimate that a spectroscopic feature three to five times smaller than *tp*-HOONO ($3\nu_{\text{OH}}$) would be indistinguishable from baseline noise at the scan speeds required to span the search region in a reasonable time. To date, spectroscopic searches have been conducted from 8865 to 9563 cm^{-1} to look for *cc*-HOONO ($3\nu_{\text{OH}}$), with the broad scan range being dictated by an earlier study under thermal conditions.²⁰

VI. CONCLUSIONS

The second OH overtone transition of *tp*-HOONO has been identified under jet-cooled conditions based on its vibrational frequency ($10\,195.3\text{ cm}^{-1}$) and rotational band structure. When combined with analogous measurements for the first overtone transition of *tp*-HOONO,^{11,22} the OH local mode can be characterized by a harmonic frequency of $\omega_e = 3747.5\text{ cm}^{-1}$ and an anharmonicity of $\omega_e x_e = 87.3\text{ cm}^{-1}$. While the band contour for the second overtone could be simulated using rotational constants derived from the first overtone spectrum,¹¹ the *a*:*c* ratio of the transition-type is shown to change with increasing OH stretch excitation. This is indicative of charge redistribution within *tp*-HOONO (Ref. 38) that results in the transition dipole moment shifting from 35° to 49° with respect to the OH bond axis from the first to second OH overtone transition. The spectral linewidths demonstrate that the initial stage of IVR occurs about a factor of two faster for $3\nu_{\text{OH}}$ as compared with $2\nu_{\text{OH}}$ excitation of *tp*-HOONO. The second overtone is shown to be more than an order of magnitude (~ 14 -fold) weaker than the first OH overtone transition of *tp*-HOONO.

The nascent quantum state distribution of the OH ($\nu = 1$) and ($\nu = 0$) products from unimolecular dissociation of *tp*-HOONO ($3\nu_{\text{OH}}$) has been measured and, along with that

previously observed for *tp*-HOONO ($2\nu_{\text{OH}}$),¹¹ compared with the results of three different statistical models, namely, a prior distribution (prior), phase-space theory (PST), and the separate statistical ensembles (SSE) model. All of the experimental results are consistent with a previously determined binding energy for *tp*-HOONO of $D_0 = 5667(38)\text{ cm}^{-1}$ or $16.2(1)\text{ kcal mol}^{-1}$.¹¹ The OH ($\nu = 0$) rotational distributions from *tp*-HOONO ($2\nu_{\text{OH}}$ or $3\nu_{\text{OH}}$) peak at low J_{OH} and extend to the energetic limits dictated by the excitation frequency and binding energy. By comparing with the OH ($\nu = 0$) product state distributions predicted from the three different statistical models, the experimental distributions are shown to be statistical, with no lambda-doublet or spin-orbit propensities. The OH ($\nu = 0$) distributions show no evidence of an angular momentum constraint or any type of barrier moderating the dissociation dynamics of *tp*-HOONO ($2\nu_{\text{OH}}$ or $3\nu_{\text{OH}}$).

Vibrationally excited OH ($\nu = 1$) is shown to be a very small fraction of the products from *tp*-HOONO ($3\nu_{\text{OH}}$), both experimentally and as predicted from the statistical theories. Nevertheless, the relative amount of OH ($\nu = 1$) vs ($\nu = 0$) fragments can be used to distinguish between the various statistical models. The SSE model provides the best representation of the OH $X^2\Pi_{3/2}(\nu = 1)/(\nu = 0)$ population ratio observed in specific reference channels, as expected based on its formulation, and indicates that less than 2% of the OH fragments will be vibrationally excited. In addition, the statistical calculations predict that the higher energy $\text{HO}_2 + \text{NO}$ channel (as yet unobserved) will make a significant contribution (21.5%) to the total product yield from *tp*-HOONO ($3\nu_{\text{OH}}$).

ACKNOWLEDGMENTS

This research was sponsored by the Chemistry Division of the National Science Foundation. One of the authors (T.A.S.) is a recipient of a Eugene M. Lang Faculty Fellowship from Swarthmore College in support of his 2004-2005 academic year sabbatical leave. The authors thank Mychel E. Varner and John F. Stanton (University of Texas at Austin) for sharing the results of their $3\nu_{\text{OH}}$ calculations for HOONO prior to publication. We also acknowledge helpful discussions with group members Ilana B. Pollack and Craig R. Murray.

¹B. J. Finlayson-Pitts and J. N. Pitts, *Chemistry of the Upper and Lower Atmosphere: Theory, Experiments, and Applications* (Academic, San Diego, 2000).

²D. M. Golden and G. P. Smith, *J. Phys. Chem. A* **104**, 3991 (2000).

³N. M. Donahue, R. Mohrschlatt, T. J. Dransfield, J. G. Anderson, and M. K. Dubey, *J. Phys. Chem. A* **105**, 1515 (2001).

⁴H. Hippler, S. Nasterlack, and F. Striebel, *Phys. Chem. Chem. Phys.* **4**, 2959 (2002).

⁵D. M. Golden, J. R. Barker, and L. L. Lohr, *J. Phys. Chem. A* **107**, 11057 (2003).

⁶J. S. Robertshaw and I. W. M. Smith, *J. Phys. Chem.* **86**, 785 (1982).

⁷J. B. Burkholder, P. D. Hammer, and C. J. Howard, *J. Phys. Chem.* **91**, 2136 (1987).

⁸M. P. McGrath and F. S. Rowland, *J. Phys. Chem.* **98**, 1061 (1994).

⁹D. A. Dixon, D. Feller, C.-G. Zhan, and J. S. Francisco, *J. Phys. Chem. A* **106**, 3191 (2002).

¹⁰B. D. Bean, A. K. Mollner, S. A. Nizkorodov, G. Nair, M. Okumura, S. P. Sander, K. A. Peterson, and J. S. Francisco, *J. Phys. Chem. A* **107**,

- 6974 (2003).
- ¹¹I. M. Konen, I. B. Pollack, E. X. J. Li, M. I. Lester, M. E. Varner, and J. F. Stanton, *J. Chem. Phys.* **122**, 094320 (2005).
- ¹²I. Matthews and A. Sinha, *J. Chem. Phys.* **122**, 104313 (2005).
- ¹³J. Fry, S. A. Nizkorodov, M. Okumura, C. M. Roehl, J. S. Francisco, and P. O. Wennberg, *J. Chem. Phys.* **121**, 1432 (2004).
- ¹⁴M. P. McGrath and F. S. Rowland, *J. Chem. Phys.* **122**, 134312/1 (2005).
- ¹⁵D. P. Schofield and H. G. Kjaergaard, *J. Phys. Chem. A* **109**, 1810 (2005).
- ¹⁶A. B. McCoy, J. L. Fry, J. S. Francisco, A. K. Mollner, and M. Okumura, *J. Chem. Phys.* **122**, 104311 (2005).
- ¹⁷B. M. Cheng, J. W. Lee, and Y. P. Lee, *J. Phys. Chem.* **95**, 2814 (1991).
- ¹⁸W.-J. Lo and Y. P. Lee, *J. Chem. Phys.* **101**, 5494 (1994).
- ¹⁹S. A. Nizkorodov and P. O. Wennberg, *J. Phys. Chem. A* **106**, 855 (2002).
- ²⁰J. Matthews, A. Sinha, and J. S. Francisco, *J. Chem. Phys.* **120**, 10543 (2004).
- ²¹B. J. Drouin, J. L. Fry, and C. E. Miller, *J. Chem. Phys.* **120**, 5501 (2004).
- ²²I. B. Pollack, I. M. Konen, E. X. J. Li, and M. I. Lester, *J. Chem. Phys.* **119**, 9981 (2003).
- ²³L. S. Rothman, C. P. Rinsland, A. Goldman *et al.*, *J. Quant. Spectrosc. Radiat. Transf.* **60**, 665 (1998).
- ²⁴G. H. Dieke and H. M. Crosswhite, *J. Quant. Spectrosc. Radiat. Transf.* **2**, 97 (1962).
- ²⁵J. Luque and D. R. Crosley, LIFBASE: database and spectral simulation, Version 1.5, SRI International Report No. MP 99, 1999.
- ²⁶D. R. Yarkony, *J. Chem. Phys.* **97**, 1838 (1992).
- ²⁷G. Parlant and D. R. Yarkony, *J. Chem. Phys.* **110**, 363 (1999).
- ²⁸J. M. Hossenlopp, D. T. Anderson, M. W. Todd, and M. I. Lester, *J. Chem. Phys.* **109**, 10707 (1998).
- ²⁹I. M. Konen and M. I. Lester (unpublished).
- ³⁰G. Herzberg, *Molecular Spectra and Molecular Structure: Spectra of Diatomic Molecules* (Van Nostrand, New York, 1950).
- ³¹K. J. Feierabend, D. K. Havey, and V. Vaida, *Spectrochim. Acta, Part A* **60A**, 2775 (2004).
- ³²P. R. Fleming, M. Li, and T. R. Rizzo, *J. Chem. Phys.* **94**, 2425 (1991).
- ³³D. J. Donaldson, J. J. Orlando, S. Amann, G. S. Tyndall, R. J. Proos, B. R. Henry, and V. Vaida, *J. Phys. Chem. A* **102**, 5171 (1998).
- ³⁴A. Sinha, R. L. Vander Wal, and F. F. Crim, *J. Chem. Phys.* **92**, 401 (1990).
- ³⁵A. Sinha, R. L. Vander Wal, and F. F. Crim, *J. Chem. Phys.* **91**, 2929 (1989), and references cited therein.
- ³⁶J. A. Coxon, *Can. J. Phys.* **58**, 933 (1980).
- ³⁷K. Takahashi, M. Sugawara, and S. Yabushita, *J. Phys. Chem. A* **109**, 4242 (2005).
- ³⁸T. A. Stephenson, I. M. Konen, and M. I. Lester (unpublished).
- ³⁹Using phase-space theory (PST), the fraction of OH products in the specified product state, $\nu=0$, $J_{\text{OH}}=9/2$, $\Omega=3/2$, $\Pi(A'')$, was 0.061 for tp-HOONO ($3\nu_{\text{OH}}$) and 0.117 for ($2\nu_{\text{OH}}$). The separate statistical ensembles (SSE) model yields similar fractional populations. See Sec. IV for a description of the statistical models.
- ⁴⁰Using PST to estimate the branching fraction for the HO₂+NO product channel (see Sec. IV) reduces the oscillator strength ratio to ~ 11 .
- ⁴¹R. G. Gilbert and S. C. Smith, *Theory of Unimolecular and Recombination Reactions* (Blackwell Scientific, Oxford, 1990).
- ⁴²T. Baer and W. L. Hase, *Unimolecular Reaction Dynamics* (Oxford University Press, New York, 1996).
- ⁴³M. Hunter, S. A. Reid, D. C. Robie, and H. Reisler, *J. Chem. Phys.* **99**, 1093 (1993).
- ⁴⁴C. Wittig, I. Nadler, H. Reisler, M. Noble, J. Catanzarite, and G. Radhakrishnan, *J. Chem. Phys.* **83**, 5581 (1985).
- ⁴⁵H. D. Bist and J. C. D. Brand, *J. Mol. Spectrosc.* **62**, 60 (1976).
- ⁴⁶J. Zhang, T. Dransfield, and N. M. Donahue, *J. Phys. Chem. A* **108**, 9082 (2004).
- ⁴⁷J. D. DeSain, A. D. Ho, and C. A. Taatjes, *J. Mol. Spectrosc.* **219**, 163 (2003).
- ⁴⁸J. B. Burkholder, P. D. Hammer, C. J. Howard, J. P. Towle, and J. M. Brown, *J. Mol. Spectrosc.* **151**, 493 (1992).
- ⁴⁹J. M. Brown, A. R. H. Cole, and F. R. Honey, *Mol. Phys.* **23**, 287 (1972).
- ⁵⁰J. Almlöf and P. R. Taylor, *J. Chem. Phys.* **86**, 4070 (1987).
- ⁵¹M. E. Varner and J. F. Stanton (private communication).
- ⁵²The state count neglected Coriolis coupling and treated the HOON torsion as a hindered rotor in a sinusoidal well with a well-defined fundamental frequency and reduced moment of inertia. The anharmonic frequency state count was performed using the MULTIWELL program suite.
- ⁵³J. R. Barker, N. F. Ortiz, J. M. Preses, and L. L. Lohr, MULTIWELL-1.4.1 software, <http://aoss.engin.umich.edu/multiwell/> (2004).
- ⁵⁴J. R. Barker, *Int. J. Chem. Kinet.* **33**, 232 (2001).
- ⁵⁵P. R. Stannard and W. M. Gelbart, *J. Phys. Chem.* **85**, 3592 (1981).
- ⁵⁶K. K. Lehmann, G. Scoles, and B. H. Pate, *Annu. Rev. Phys. Chem.* **45**, 241 (1994).
- ⁵⁷D. J. Nesbitt and R. W. Field, *J. Phys. Chem.* **100**, 12735 (1996).
- ⁵⁸K. Doclo and U. Rothlisberger, *Chem. Phys. Lett.* **297**, 205 (1998).
- ⁵⁹Y. Zhao, K. N. Houk, and L. P. Olson, *J. Phys. Chem. A* **108**, 5864 (2004).